MICROWAVE HEAD IMAGING FOR STROKE DETECTION

D. Ireland* and M. Bialkowski

School of ITEE, University of Queensland St. Lucia, Brisbane, Australia

Abstract—This paper proposes an algorithm for wide-band microwave imaging for the detection of a hemorrhagic stroke. A realistic head phantom and finite-difference time-domain program are used to estimate back-scattered signals which are subsequently used in the image reconstruction process. The proposed imaging approach can lead to a portable and cost effective system; particularly suitable for rural medical clinics that lack the necessary resources in effective stroke diagnosing.

1. INTRODUCTION

Microwave imaging for brain abnormalities has recently been proposed [1–3]. The underlying notion of the technique is based on recent studies that demonstrated tissue malignancies, blood supply, hypoxia, acute ischemia, and chronic infarction significantly change dielectric properties of the effected tissue [2, 4]. Probing the brain works by exposing tissues to low-levels of electromagnetic energy at microwave frequencies and capturing the scattered electromagnetic energy. Subsequently the estimation of the dielectric profiles of the imaged body are constructed or significant scatterers are directly located. The latter approach has been widely used in breast cancer detection using microwave imaging [5–8]. In this paper we apply this approach for the detection of a brain stroke.

A stroke is a disturbance in the blood supply to the brain caused by either a blocked or burst blood vessel. Brain tissue is subsequently

* Corresponding author: David Ireland (david.ireland@uq.edu.au).

denied oxygen and glucose resulting in rapid loss of brain functions and often death. Strokes are the leading cause of adult disability in the world and are the number two cause of death worldwide [9]. A stroke can be cast into two major categories, ischemic and hemorrhagic. An acute ischemic stroke is where blood supply to part of the brain is decreased by thrombosis (obstruction of a blood vessel by a blood clot forming locally) or an embolism (obstruction due to an embolus from elsewhere in the body). A hemorrhagic stroke occurs when a blood vessel bursts inside the brain; the blood accumulates and compresses the surrounding brain tissue.

A patient suffering from a suspected stroke is a medical emergency. The course of treatment for ischemic and haemorrhagic stroke is vastly different. Lethal consequences could occur if the stroke is not properly classified before beginning treatment. The symptoms of a stroke are varied and include: difficulty swallowing, weakness or clumsiness, slurred speech, difficulty with reading, dizziness and an altered feeling on one side [10]. The resultant differential diagnoses are also varied and include: migraine, epilepsy, syncope, intra-cranial structural lesions and multiple sclerosis [10].

An initial examination done by a physician is typically clinical using a neurological exam. This however is not always conclusive as many non-vascular conditions can simulate stroke symptoms. In contrast, so-called stroke *chameleons* are strokes that present with uncommon symptoms. A recent study found that 21% of patients thought to have had an anterior circulation ischemic stroke at initial clinical evaluation had in fact suffered from either another type of stroke or a non-vascular condition [11]. As such, physicians primarily rely on medical imaging systems such as the computed tomography (CT) scan and magnetic resonance imaging (MRI) for confirmation of the diagnosis. The complexity of stroke diagnosis emphasizes the vital importance played by the CT and MRI scan systems. They are however, not fast, cost effective or portable, nor are they accessible at rural medical clinics, or carried by first response paramedical teams. Potentially, microwave imaging can supplement current diagnostic methods as it may potentially provide a fast, cost effective and portable detection system [2].

The aim of this paper is to provide initial results as to the efficacy of microwave imaging for hemorrhagic stroke detection This is done using an anatomically realistic head phantom, and a 2-D finite-difference time domain (FDTD) method to predict the scattered electromagnetic fields.

2. SIMULATION MODEL

2.1. Head Phantom

The basis of this work involves the use of a realistic head phantom. This phantom was obtained from [12] which originated from a detailed MRI scan. The phantom consists of $256 \times 256 \times 128$ cubical elements with dimensions of $1.1\,\text{mm} \times 1.1\,\text{mm} \times 1.4\,\text{mm}$ respectively. Seven different types of tissues that includes: skin, skull, fat, blood, dura, cerebral spinal fluid (CSF), gray and white matter.. As this paper only considers a two-dimensional imaging approach, a transverse slice of the phantom at approximately 20 mm from the crown of the head was extracted from the three-dimensional phantom.

The creators of the phantom model have also made available a data-set to indicate what tissue each cells belongs too. Furthering this, the dielectric properties of biological tissue given by [13] can be used to complete the model for microwave simulations. The tissue and the associated dielectric properties used in this article are in Table 1 showing eight unique body tissues used in the phantom. The dielectric constant and conductivity profiles of the phantom are depicted in Figures 1 and 2 respectively. The emulated stroke is an elliptical object with radii of 62.7 mm and 34.1 mm. The dielectric properties of the emulated hemorrhagic stroke are equivalent to blood as given in Table 1.
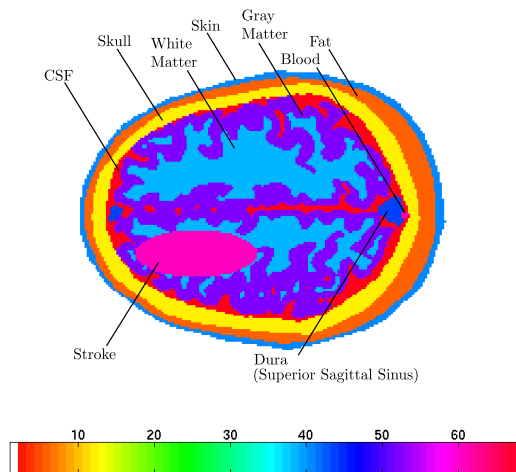

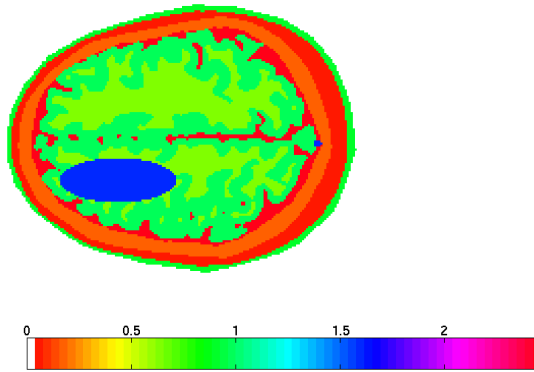**Figure 1.** Dielectric constant profile of the phantom.

Figure 2. Conductivity profiles of the phantom.

Table 1. Dielectric properties of the biological tissues used in the phantom model at 1 GHz.

Tissue	ϵ_r	σ
Skin	41	0.89977
Skull	12	0.15566
Cerebral spin fluid	68	2.4552
Gray Matter	52	0.98541
White Matter	46	0.82431
Fat	5	0.053502
Dura	44	0.9
Blood	61	1.5829
Hemorrhagic Stroke	**61**	**1.5829**

2.2. FDTD Method

The finite difference time domain was chosen as the electromagnetic field simulator for this analysis. This method is based on Faraday and Ampère's time-domain equations. In a Cartesian coordinate system (x, y, z), these are represented with six scalar equations that form an independent set of coupled relationships between the time-varying electric $(\partial E_x/\partial t, \partial E_y/\partial t, \partial E_z/\partial t)$ and magnetic fields $(\partial H_x/\partial t, \partial H_y/\partial t, \partial H_z/\partial t)$. The FDTD method resolves these equations in the time domain by applying central differences to the time and space derivatives. The fields at a future time are thus computed from the values of a past time instant. The method runs for a finite

number of time steps which simulates the progression of the fields in time. Incorporating the phantom model into the FDTD simulator is done quite simply by matching the same element size; thus in the FDTD, $\Delta x = 1.1\,\text{mm}$, $\Delta y = 1.1\,\text{mm}$ and the number of cells in the x and y axis was 256. The edges of the simulation domain were truncated used Liao's absorbing boundary conditions [14].

Determining the optimal spectrum in which to couple electromagnetic energy into the brain matter has yet to be adequately researched. Relatively high microwave frequencies may lack the required penetration into the brain. Lower frequencies ($< 3\,\text{GHz}$) however would allow for a higher penetration but would offer poor spatial resolution. In [2], it was asserted frequencies above $2\,\text{GHz}$ were not suitable due to the high signal attenuation; they reported successful image reconstruction using a frequency range of $0.5\,\text{MHz}$–$2\,\text{GHz}$ applied on a 2-D model with circular objects to represent a head. As such, we were inclined for our experiments to also use this bandwidth. A Gaussian pulse with bandwidth 0.5–$2\,\text{GHz}$ was used as the radiating pulse in the FDTD program.

3. IMAGING SYSTEM

Figure 3 provides an illustration on the microwave imaging system used in this paper. Here a point source resides in free-space and is rotated along an elliptical trajectory at N discrete points denoted $\mathbf{S}_i$ at position i. The point source represents a cylindrical source due to the assumption of the 2-D model. The body to be imaged is given by the gray shaded region which for later reference will be mathematically denoted $\boldsymbol{\mathcal{Z}}$ and any point inside $\boldsymbol{\mathcal{Z}}$ as $\mathbf{p}$. The outline of this body can be defined by a series of boundary points along the border circumference as illustrated in Figure 3; these points are denoted as $\{\mathbf{B}_1(x,y), \mathbf{B}_2(x,y)\ , \mathbf{B}_3(x,y), \ldots, \mathbf{B}_{N_b}(x,y)\}$ where $\mathbf{B}_i(x,y)$ is the i boundary point in Euclidean space defined by x and y coordinates, and N_b is the number of boundary points. In the case of the head phantom, the boundary points represent the skin layer.

3.1. Confocal Algorithm

This section details a confocal algorithm based on a delay-and-sum approach used in the image reconstruction. Confocal algorithms are used extensively in ultra-wideband breast imaging, notable examples include [15–17]. The confocal algorithm works by making a hypothesis that an echo signal originates from a given point; the normalized difference signals of each antenna are added at this space location.
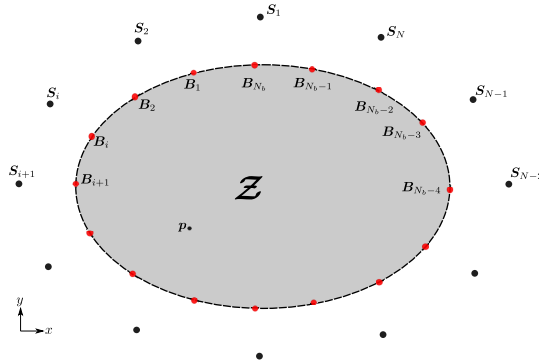
Figure 3. Illustration of the microwave imaging setup. The gray region represents the body to be imaged denoted $\mathcal{Z}$. Boundary points denoted $\mathbf{B}_i(x, y)$ represent discrete points in space between the body to be imaged and free-space. Any discrete point inside is denoted $\mathbf{p}$.

If the hypothesis for the particular scatterer location is correct, the signals add coherently and a large value of the sum is obtained. If the hypothesis is incorrect, the signals add incoherently and the sum is small. The signals are postulated to travel in straight lines. Strictly speaking, this requires an assumption that the propagating medium is homogeneous. This is not the case. Therefore it is expected that an assumption will lead to errors in locating the targeted scattering object. It is apparent that to implement this concept, some information about the dielectric constant of the propagation is constant. In this analysis we assume the average dielectric constant, denoted $\bar{\epsilon}$, is 37. This value was obtained from knowledge of the dielectric profiles of the phantom.

Before the confocal process can be applied, it is necessary to perform the following pre-processing steps:

 (i) Obtain N antenna time-domain signals $A_n(t)$ where $n = 1, 2, \ldots, N$. These signals contain the echo signals.

(ii) Construct difference signals to cancel out any common background signals (e.g., skin layers). $D_n(t) = A_n(t) - A_{n+1}(t)$ for $n = 1, 2, \ldots, N-1$ and $D_N(t) = A_N(t) - A_1(t)$.

(iii) Compensate for signals losses by $F_n(t) = D_n(t)y(t)$ where $n = 1, 2, \ldots, N$ and $y(t)$ is the compensation factor. At present the authors use:

$$y(t) = \frac{1}{e^{-\alpha t}} \qquad (1)$$

were α adjusts the slope of the compensation function. Further on the effect of this value in the reconstructed image is shown.

How we test the hypothesis is paramount in obtaining an accurate image. We must determine the correct path the wave-front travels and have a reasonable knowledge of the dielectric and magnetic properties of the medium the waves travel in. In order to estimate the path of the wave took, we have made use of Fermat's principle which states the path that minimises the travel time is the real path.

Algorithm 1 gives the pseudo-code for our confocal imaging algorithm. Here we implement Fermat's principle by constructing all possible propagation paths from the antenna to the boundary points, and then from the boundary points to the current point in **p**. Accordingly our optimal path is the minimal electrical distance. We then obtain the time index according to the electrical distance and the velocity of light. The function denoted [•] rounds to the nearest integer allowing elements to be accessed in the array of data. A continuous colour image is produced using a shading operator to interpolate at non-tested points. Strong intensity colours indicate the location of significant scattering objects. For further details on the development and variations of this algorithm the reader is refereed to [7, 8, 18].

Algorithm 1: Monostatic Confocal imaging algorithm.

> **begin**
> > **for** $n \leftarrow 1$ **to** N **do**
> > > **for** $\forall p \in \mathcal{Z}$ **do**
> > > > **for** $d \leftarrow 1$ **to** N_b **do**
> > > > > $D_d \leftarrow ||S_n - B_d|| + \sqrt{\epsilon}||p - B_d||$
> > > >
> > > > $d \leftarrow \min\{D_1, D_2, \ldots, D_{N_b}\}$
> > > > $\tau \leftarrow [2 \times d/c]$
> > > > $I(p) \leftarrow I(p) + |F_n(\tau)|$

3.2. Metrics

Quantitative metrics are convenient to quantify the performance of the imaging algorithm In order to define the metrics used in this paper it is necessary first to define a further set of points that map to the location of the emulated stroke in the phantom. These collection of points are denoted $\mathcal{T}$. The first metric is the ratio of the average intensity value of points located in the stroke region over the points in the remaining tissues. Given as:

$$Q = \frac{\mu\left[I\left(\mathbf{p}\right)\right]}{\mu\left[I\left(\mathbf{p}\right)\right]} \quad \begin{array}{l} \forall \mathbf{p} \in \mathcal{T} \\ \forall \mathbf{p} \notin \mathcal{T} \end{array} \tag{2}$$

where $\mu[\bullet]$ denotes the mean function. A higher value for this metric implies the stroke intensity is more intensive than the background regions. The second metric is the ratio of the maximum intensity value of the stroke region over the maximum intensity of the complete image. Given as:

$$\gamma = \frac{\max\left[I\left(\mathbf{p}\right)\right]}{\max\left[I\left(\mathbf{p}\right)\right]} \quad \begin{array}{l} \forall \mathbf{p} \in \boldsymbol{\mathcal{T}} \\ \forall \mathbf{p} \in \boldsymbol{\mathcal{Z}} \end{array} \tag{3}$$

The third metric is the absolute distance between the central location of the stroke and the location of the maximum intensity given in the reconstructed image. If $\mathbf{t}$ denotes the point of the centre of the tumor, then this metric is defined as:

$$E = \left\| \mathbf{p}^* - \mathbf{t} \right\| \tag{4}$$

where:

$$\mathbf{p}^* = \arg\max_{\mathbf{p} \in \mathcal{Z}} \left\{ I\left(\mathbf{p}\right) \right\} \tag{5}$$

4. RESULTS

4.1. Head Phantom

For the first experiment, a healthy head phantom is simulated. A Gaussian pulse with a 0.5–2 GHz bandwidth is excited and the back-scattered signals captured at 72 antenna positions surrounding the phantom. The signals are quantised to 16-bits as most commercially available analogue-to-digital converters are limited to 16-bits. White noise is subsequently added to produce a signal with 20 dB signal-to-noise-ratio. Using the pre-processing steps from Section 3.1 and algorithm 1, images are reconstructed from the simulated back-scattered signals for when the phantom has no stroke. This is done when $\alpha = 1$, 0.1, 0.05 and 0.025. Figure 4 gives the reconstructed images for each case in the form of a heat-map where red colours represent a more reflective scatterer and the blue colours minimal electromagnetic scattering. The images show α has a direct influence on the images. In particular, the focal region radially decreases in the image. Table 2 gives the mean image intensities for each tissue type, that is $\mu\left[I\left(\mathbf{p}\right)\right]$ for when $\mathbf{p} \in$ skin, fat, skull, dura blood, CSF, gray matter, white matter. Evidently with $\alpha = 1$, the dura, blood, skin, skull and fat are comparable scatterers. When $\alpha = 0.01$ the comparable scatterers become the dura, blood and CSF. As α decreases to 0.05 and 0.025, the comparable scatterers become the white/gray matter, dura, blood and CSF.

Table 2. Mean image intensities of each tissue at different values of α. Tissue values in bold are the strongest electromagnetic scatterers.

α	Skin	Skull	Fat	Dura	Blood	CSF	Gray Matter	White Matter
1	0.525	0.527	0.532	0.531	**0.627**	0.465	0.30	0.174
0.1	0.239	0.291	0.260	0.570	**0.673**	0.406	0.356	0.247
0.05	0.191	0.207	0.204	**0.400**	0.386	0.263	0.323	0.360
0.025	0.245	0.263	0.260	0.362	0.375	0.309	0.365	**0.465**

(a) $\alpha = 1$

(b) $\alpha = 0.1$
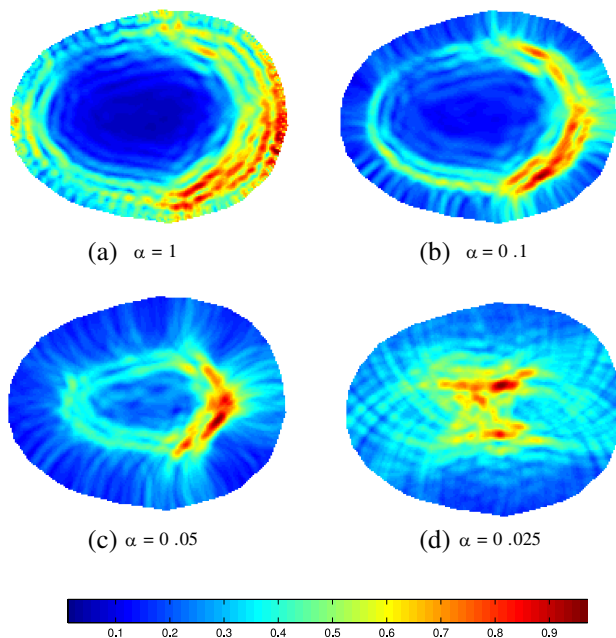
(c) $\alpha = 0.05$

(d) $\alpha = 0.025$

Figure 4. Reconstructed images for a healthy phantom with different values of α. Red colours represent more reflective scatterer and the blue colours minimal electromagnetic scattering.

4.2. Head Phantom with Stroke

In the second experiment the emulated stroke is included in the simulation. Again the excited pulse has 0.5–2 GHz bandwidth and the back-scattered signals quantised to 16-bits and noise added to obtain a signal with 20 dB SNR. Figure 5 provides reconstructed images. Four different stroke positions are shown with the central locations given by the cross-hairs. α is set to 0.025 as it was previously shown gray/white

matter are the strongest scatterers with this compensation function. Table 3 quantifies the images produced by the algorithm according to the metric functions as given in Section 3.2. From Figure 5 and Table 3, it is apparent the stroke region has a higher intensity compared to the remaining tissue regions. This is supported by Q values greater than 1 in Table 3. Images in Figures 5(a), (b) and (d) showed the maximum heat-map intensity occurred in the stroke region as $\gamma = 1$ for these
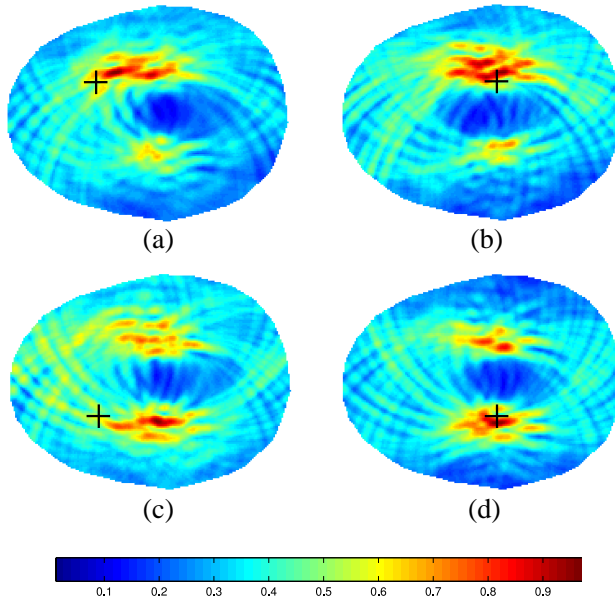

Figure 5. Reconstructed images for when the emulated stroke is included in the FDTD simulation and $\alpha = 0.025$. Four different stroke positions are shown with the central locations given by the cross-hairs. Red colours represent more reflective scatterer and the blue colours minimal electromagnetic scattering.

Table 3. Performance of the reconstruction algorithm in detecting four different stroke locations with respect to Figure 5.

Image Figure	Q	γ	E [mm]
(a)	1.58	1.00	15.8
(b)	1.63	1.00	6.40
(c)	1.26	0.82	40.0
(d)	1.65	1.00	5.68

cases. The corresponding E metric shows location errors of 15.8 mm, 6.40 mm and 5.68 mm respectively. Figure 4(c) produced the largest E error of 40 mm.

5. CONCLUSION

This paper has described an image reconstruction algorithm for the purpose of detecting a haemorrhagic stroke. The algorithm uses the scattering signal data when a pulse signal of 0.5–2 GHz is transmitted. Its efficacy was tested used a realistic head phantom and estimated back-scatter signals from a FDTD program. Images reconstructed using back-scattered signals from a healthy head phantom are initially presented. A focal region is seen to be adjustable via a parameter in the exponential compensation factor. This parameter has the effect of varying the radii of the confocal region. Further on images are constructed from back-scattered signals from a head phantom with an emulated stroke. Four different stroke positions are tested with accurate reconstructed images in all cases except one.

Future work will include testing the algorithms ability in imaging other types of strokes and intra-cranial diseases.

ACKNOWLEDGMENT

REFERENCES

1. Ireland, D. and M. E. Bialkowski, "Feasibility study on microwave stroke detection using a realistic phantom and the FDTD method," *Asia Pacific Microwave Conference*, 1360–1363, Yokohama, Japan, December 2010.

2. Serguei, Y., Y. Semenov, and D. R. Corfield, "Microwave tomography for brain imaging: Feasibility assessment for stroke detection," *International Journal of Antennas and Propagation*, Vol. 2008, Article ID 254830, 8, 2008, doi:10.1155/2008/254830.

3. Trefnam, H. and M. Persson, "Antenna array design for brain monitoring," *Antennas and Propagation Society International Symposium, (AP-S 2008)*, San Diego, Ca, Jul. 2008.

4. Semenov, S. Y., R. H. Svenson, V. G. Posukh, A. G. Nazarov, Y. E. Sizov, A. E. Bulyshev, A. E. Souvorov, W. Chen, J. Kasell, and G. P. Tatsis, "Dielectrical spectroscopy of canine myocardium

during acute ischemia and hypoxia at frequency spectrum from 100 kHz to 6 GHz," *IEEE Transactions on Medical Imaging*, Vol. 21, No. 6, Jun. 2002.

5. Khor, W. C., A. A. Bakar, and M. E. Bialkowski, "Investigations into breast cancer detection using ultra wide band microwave radar technique," *Asia Pacific Microwave Conference*, 712–715, Singapore, Dec. 7–10, 2009.

6. Bialkowski, M. E., D. Ireland, Y. Wang, and A. Abbosh, "Ultra-wideband array antenna system for breast imaging," *Asia Pacific Microwave Conference*, 267–270, Yokohama, Japan, Dec. 2010.

7. Bialkowski, M. E. and Y. Wang "UWB cylindrical microwave imaging system employing virtual array antenna concept for background effect removal," *Microwave and Optical Technology Letters*, Vol. 53, No. 5, 1100-4, May 2011.

8. Bialkowski, M. E., "Ultra wideband microwave system with novel image reconstruction strategies for breast cancer detection," *EuMC2010: 40th European Microwave Conference 2010*, 537–540, Paris, France, Sep. 2010.

9. Feigin, V., "Stroke epidemiology in the developing world," *The Lancet*, Vol. 365, No. 9478, 2160–2161, Jun. 2005.

10. Ma, H., J. Ly, and G. A. Donnan, "TIA and stroke: A management guide for GPs," *Medicine Today*, Vol. 7, No. 5, May 2006.

11. Libman, R. B., E. Wirkowski, J. Alvir, and T. H. Rao, "Conditions that mimic stroke in the emergency department. Implications for acute stroke trials," *Archives of Neurology*, 1119–1122, 1995.

12. Zubal, I. G., C. R. Harrell, E. O. Smith, Z. Rattner, G. Gindi, and P. B. Hoffer, "Computerized three-dimensional segmented human anatomy," *Medical Physics*, Vol. 21, No. 2, 299–302, 1994.

13. "Dielectric properties of body tissues in the frequency range 10 Hz–100 GHz," Available: http://niremf.ifac.cnr.it/tissprop/, May 26, 2010.

14. Liao, Z. P., H. L. Wong, B. P. Yang, and Y. F. Yuan, "A transmitting boundary for transient wave analysis," *Scientia Sinica A*, Vol. 27, 10631076, 1984.

15. O'Halloran, M., M. Glavin, and E. Jones, "Rotating antenna microwave imaging system for breast cancer detection," *Progress In Electromagnetics Research*, Vol. 107, 203–217, 2010.

16. Zhu, G. K. and M. Popovic, "Comparison of radar and thermoacoustic technique in microwave breast imaging," *Progress*

In Electromagnetics Research B, Vol. 35, 1–14, 2011.

17. Xu, L. and S. C. Hagness, "A confocal microwave imaging algorithm for breast cancer detection," *IEEE Microwave and Wireless Components Letters*, Vol. 11, No. 3, March 2001.

18. Bialkowski, M. E., Y. Wang, A. A. Bakar, and W. C. Khor, "Novel image reconstruction algorithm for a UWB cylindrical microwave imaging system," *IMS2010 Digest*, 1–4, Anaheim, California, USA, May 23–28, 2010.